J Sci Comput (2015) 63:330–354
DOI 10.1007/s10915-014-9895-0

A Sharp Computational Method for the Simulation of the Solidification of Binary Alloys

Maxime Theillard · Frédéric Gibou · Tresa Pollock

Received: 19 September 2013 / Revised: 13 July 2014 / Accepted: 16 July 2014 /
Published online: 5 August 2014

Abstract We present a numerical method for the simulation of binary alloys. We make use of the level-set method to capture the evolution of the solidification front and of an adaptive mesh refinement framework based on non-graded quadtree grids to efficiently capture the multiscale nature of the alloys' concentration profile. In addition, our approach is based on a sharp treatment of the boundary conditions at the solidification front. We apply this algorithm to the solidification of an Ni–Cu alloy and report results that agree quantitatively with theoretical analyses. We also apply this algorithm to show that solidification mechanism maps predicting growth regimes as a function of tip velocities and thermal gradients can be accurately computed with this method; these include the important transitions from planar to cellular to dendritic regimes.

Keywords Solidification · Binary alloy · Dendritic growth · Sharp model · Stefan problem · Non-graded adaptive grid · Quadtree

1 Introduction

Metallic materials are at the core of a broad array of advanced engineering systems, with a total global production of greater than a billion tons annually [1]. One of the grand challenges for computational materials science is the development of a true predictive capability for the structure and properties of metallic systems—through all the stages of processing and into

M. Theillard (✉)
Mechanical Engineering Department, University of California, Santa Barbara, CA 93106, USA
e-mail: maxime@engineering.ucsb.edu

F. Gibou
Mechanical Engineering Department and Computer Science Department, University of California, Santa Barbara, CA 93106, USA

T. Pollock
Materials Department, University of California, Santa Barbara, CA 93106, USA

the service environment. Since the vast quantity of all metallic systems undergo melting and solidification early in their life cycle, models that accurately capture the solute segregation and defects that may form during solidification is an essential first step. An example of industrial importance where the most advanced degree of control of solidification is key is nickel-base single crystals. These multicomponent single crystals are critical to virtually all gas turbine systems in the energy and aerospace industries, where single crystals ranging in mass from less than 1 kg up to 30 kg must be solidified. [2–5]. The processes of choice may either be the conventional Bridgman process or the more recent liquid metal cooling (LMC) technique, where the melt is slowly withdrawn from the hot zone of the furnace into a bath of liquid tin [4,6,7].

The life and performance of superalloy single crystals is typically limited by defects that form during solidification [4,5,8–10]. These include solidification-induced pores, phases that precipitate due to strong solidification segregation or small grains that form due to convection-induced fragmentation of the dendritic structure during withdrawal. Understanding the formation and minimizing the occurrence of these features during solidification is critical to the development of new materials and their deployment into new systems. In addition, solidification mechanism maps predicting growth regimes as a function of thermal gradients and front velocities are used extensively in the development of solidification processing conditions for new alloys and/or new single crystal component designs. To date, these maps have been partially or fully developed experimentally at great expense. Making this capability available to industry could profoundly accelerate process development cycles and expand the sets of materials that they could incorporate into their processes—not only for investment cast materials, but across the entire spectrum of industrial casting processes. Finally, while there is an ongoing need for new Ni-base alloys, the time and cost of development has become prohibitive. This is an area where New Integrated Computational Materials Engineering (ICME) approaches hold great promise for accelerating development and predicting performance could significantly impact the design of advanced materials and the energy efficiency of both power generation systems and aircraft engines.

Efficient computational approaches therefore hold great promise for accelerating development and predicting performance, but are challenged when multicomponent materials must be analyzed. The growth is driven by heat and mass transfer, convective effects of fluid flows as well as the effects of capillary forces, crystallographic anisotropy, thermodynamics and kinetics [11–16]. In addition, the solidification front is time dependent and, depending on the scale at which the solidification processes are studied, physically correct boundary conditions must be imposed *at* the moving front. Indeed, when viewed on an *atomistic* scale, the solidification front is seen to be a region where the solute concentration undergoes rapid but continuous variations. Hence, in an atomistic theory, and in turn at the scale where atomistic computations are feasible, boundary conditions would not be necessary and a continuous concentration profile would be physically correct. When viewed with the much coarser resolution of the macroscopic description, on the other hand, these local variations can be distinguished only as discontinuities. In the case of the study of dendritic growth, the characteristic length scale of the dendrites is macroscopic and therefore imposes the use of the continuum approximation. In turn, the correct physical model is that where the concentration is discontinuous at the solidification front. This is the so-called *sharp* interface model that is universally accepted as the physically correct model for dendritic growth [11]. It is therefore necessary that a *sharp* numerical treatment of the boundary conditions be imposed.

We note that the physically correct continuous variation of the solute's concentration at the atomistic scale is to be distinguished from numerical approximations that use an artificial smearing of the concentration field as a means to avoid the difficult numerical treatment of

sharp boundary conditions. Many such approaches exist in the literature, including the phase-field method [17–36], delta formulations used in the front tracking methodology [37,37–41], homogenization or smooth particle hydrodynamic techniques [42,43], finite element methods [38,39,44,44–47] or the level-set techniques, with the recent work of Zabbaras et al. [48–50] being probably the current state-of-the-art. Although such numerical approximations have produced interesting results, it is important to note that such numerical smearings may not be accurate approximations of the underlying physics since, even though the sharp interface model is accurately approximated when the phase-field thickness parameter approaches zero, this theoretical limit is not reached on grids with cell sizes orders of magnitude larger than the physical diffuse interface.

In this paper, we present a numerical method that approximate the sharp interface model. We build on the adaptive mesh refinement framework of Min, Gibou and Chen [51–53], who presented a method to solve the standard Stefan problem where only one materials component is considered (hence only the temperature field is computed). The present work is a computational approach to the simulation of the solidification of binary alloys that demands that the concentration be computed in addition to the temperature field, that jump conditions be imposed at the solidification front and that the interplays between the temperature and concentration fields be taken into account.

2 Physical Model

Consider a domain Ω, decomposed into two subdomains Ω^s and Ω^l corresponding to the solid and liquid phases, respectively and denote by Γ the solid–liquid interface (Fig. 1). The dynamic of dendritic growth can be viewed as a nonlinear Stefan-type problem in which the evolution of the solute's concentration, C, and the temperature, T, satisfy the following diffusion equations:

$$\begin{cases} \partial T/\partial t &= \lambda \Delta T &, \forall \boldsymbol{x} \in \Omega^s \cup \Omega^l, \\ \partial C^l/\partial t &= D^l \Delta C^l &, \forall \boldsymbol{x} \in \Omega^l, \\ \partial C^s/\partial t &= D^s \Delta C^s &, \forall \boldsymbol{x} \in \Omega^s, \end{cases} \tag{1}$$

We have assumed that the density ρ is constant, that the heat capacities and thermal conductivities are constant and identical in each phase and equal to c and k, respectively. We have also assumed that the solutal diffusion coefficients are constant in each phase, and equal to D^l and D^s in the liquid and solid phase, respectively. We denote $\lambda = k/\rho c$.

This system of partial differential equations needs to be completed by a set of interfacial conditions. We assume that the temperature is continuous across the solid–liquid interface:

$$[T]_{\big|\Gamma} = 0 \tag{2}$$

and that the Gibbs–Thompson relation is satisfied at the interface:

$$T_{\big|\Gamma} = T_m + m_L C^l{}_{\big|\Gamma} + \epsilon_c(\theta)\kappa + \epsilon_v V_\Gamma, \tag{3}$$

where T_m is the melting temperature, m_L is the liquidus slope, ϵ_c and ϵ_v are the curvature and kinetic undercooling coefficients with θ the angle between the principal direction and the normal to the interface (see Fig. 1), κ is the front's curvature and V_Γ is the interface's normal velocity. The anisotropy in the curvature undercooling is a direct consequence of the crystalline anisotropy and several models have been proposed in the literature [11]. For example, the most commonly used expression for a fourfold crystalline structure in two

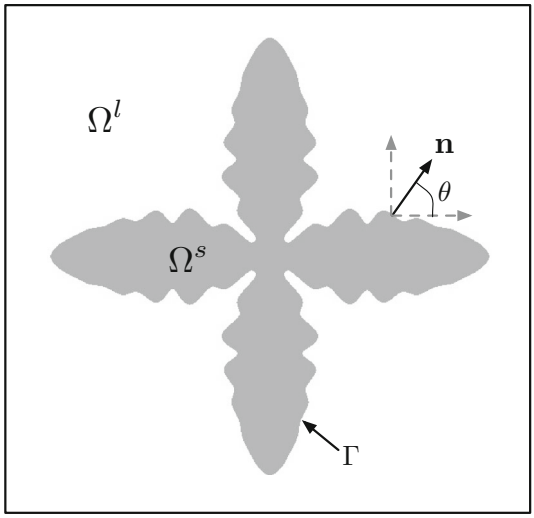

Fig. 1 Geometric configuration of a computational domain. The solid and liquid phases are represented by Ω^s and Ω^l, respectively. The solidification front, with outward normal $\boldsymbol{n}$ is denoted by Γ. The angle θ between the x-axis and the normal direction to the interface is used in defining the surface tension anisotropy

spatial dimensions is $\epsilon_c(\theta) = \epsilon_c\,(1 - 15\epsilon\cos 4\theta)$. The heat flux balance at the interface is given by:

$$V_\Gamma = \frac{k}{L}\left[\frac{\partial T}{\partial \boldsymbol{n}}\right]_\Gamma = \frac{k}{L}\left(\frac{\partial T^s}{\partial \boldsymbol{n}} - \frac{\partial T^l}{\partial \boldsymbol{n}}\right)\Big|_\Gamma, \tag{4}$$

where L is the latent heat, T^s and T^l refer to the temperature in the solid and in the liquid phases, respectively, and $\boldsymbol{n}$ is the outward normal to the solidification front (see Fig. 1). This set of conditions is supplemented by the solute-rejection equation:

$$V_\Gamma (C^s - C^l)\big|_\Gamma = D^s \frac{\partial C^s}{\partial \boldsymbol{n}}\bigg|_\Gamma - D^l \frac{\partial C^l}{\partial \boldsymbol{n}}\bigg|_\Gamma.$$

Under the assumptions that the solid concentration C^s at the interface is related to the liquid concentration C^l through the partition coefficient, k_p, as $C^s = k_p C^l$, the solute rejection equation becomes:

$$(1 - k_p) C^l V_\Gamma = D^s \frac{\partial C^s}{\partial \boldsymbol{n}}\bigg|_\Gamma - D^l \frac{\partial C^l}{\partial \boldsymbol{n}}\bigg|_\Gamma. \tag{5}$$

The system composed of the partial differential equations in (1) supplemented by the four interfacial conditions (2)–(5) define a well-posed problem.

3 Description of the Solidification Front

The solidification front is time dependent and can undergo a change in its topology when dendrites are blocked by the growth of surrounding dendrites or are fragmented due to local thermal and fluid flow conditions. Several numerical approaches exist to capture the evolution of a free boundary with their own virtues and drawbacks, as described next.

Volume of fluid methods [54–58] keep track of the mass fraction in each computational cell. The main advantage of VOF is their ability to preserve volume. A drawback often cited

is their difficulty at computing smooth curvatures, although we refer the interested reader to the recent work of [59,60].

Explicit methods such as front tracking [37,61–63] have the advantage of being accurate since the front is represented by markers with coordinates that can updated with high-order accurate ODE solvers. The main difficulty within these approaches is the treatment of topological changes.

Phase-field methods represent the solid and the liquid phases by an order parameter (or phase-field) that is constant within each phase but varies smoothly across an interfacial region of finite thickness. Phase-field methods have been used extensively in the study of dendritic growth [17–31]. The limitation of phase-field methods is that they do not approximate the sharp interface model (this would require a grid size of the order of the atomistic transition zone) and that the time step restriction is often dominated by the small width parameter. Another difficulty is in relating the phase-field and the physical parameters.

The level-set method describes the solidification front as the zero-contour of a higher dimensional Lipschitz function [64–66] and can therefore approximate the sharp interface model. A drawback of the level-set method is that it is not volume preserving and prompts the use of adaptive grids (see e.g. [51] and the references therein), special enforcement of conservation [67] or hybridization with other methods (see e.g. [68,69] and the references therein). Several efforts exist on the simulation of temperature-driven dendritic growth in the level-set framework (see e.g. [52,70–72] and the references therein). In the case of binary alloys, several authors have also used the level-set approach to keep track of the solidification front [48–50]. However, while the solidification front can be described in a sharp sense using a level-set function, it is important to note that the approximations of the temperature and diffusion fields also need to impose the sharp boundary conditions, should the sharp interface model be correctly approximated. This has been done for example with the immersed interface methods [73], which imposes the boundary conditions with a Taylor-type analysis in the interface's normal direction. Sharp treatment of the boundary conditions is also done in the ghost-fluid approach of [72,74,75], which has also been applied to the case where the grid is encoded by quadtrees in the case of the solidification of a unary system [51,76]. In [77], the authors also used the boundary treatment of [72,74] to simulate the growth of a binary system on graded quadtree grids. The work of [77] is applied to cryopreservation, in which the temperature field is assumed to be unaffected by the solidification process. In the present paper, we focus on the solidification of binary alloys, for which this assumption is invalid, as can been seen in Eqs. (1)–(5).

3.1 The Level-Set Method

The level-set method [64] represents the solidification front in two spatial dimension as the zero cross-section of a three-dimensional Lipschitz continuous function ϕ. The solidification front Γ as well as the solid and liquid phases are described as:

$$\begin{cases} \phi(x) < 0, \ \forall \boldsymbol{x} \in \Omega^s, \\ \phi(x) > 0, \ \forall \boldsymbol{x} \in \Omega^l, \\ \phi(x) = 0, \ \forall \boldsymbol{x} \in \Gamma. \end{cases}$$

The motion of the interface Γ under the normal velocity V_Γ is described by the level-set evolution equation:

$$\frac{\partial \phi}{\partial t} + V_\Gamma \, |\nabla \phi| = 0. \tag{6}$$

In this work, we also use the following reinitialization equation

$$\frac{\partial \phi}{\partial \tau} + \text{Sign}(\phi_0)\,(|\nabla \phi| - 1) = 0, \tag{7}$$

to transform an arbitrary level-set function to a signed distance function, in order to produce robust numerical approximations of the front evolution. Here τ refers to a fictitious time step. Finally, the normal to the interface $\boldsymbol{n}$ and the curvature κ are defined as:

$$\boldsymbol{n} = \frac{\nabla \phi}{|\nabla \phi|} \qquad \text{and} \qquad \kappa = \nabla \cdot \left(\frac{\nabla \phi}{|\nabla \phi|} \right).$$

4 Adaptive Mesh Refinement

In addition to being discontinuous across the interface, the solute's concentration displays a steep gradient near the interface. It is important to accurately compute the concentration in this region since it is intrinsically related to the front velocity. High resolution is therefore needed in this region, but the solution in regions farther away can be accurately captured on significantly coarser grids. In fact, the solution drops to 5 % away from its asymptotic value in a small region of size $\delta_S = 2D_L/V_\Gamma$, where D_L is the solute diffusion constant in the liquid and V_Γ is the velocity of the interface. This characterizes the multiscale nature of the solidification of superalloys. For typical growth parameters, this region is of the order of $10\mu m$ and requires that a band of about 10 grid points of size $1\mu m$ be placed near the interface to capture the variation of the concentration. The typical computational domain, chosen to simulate a few dendrites, is about 1–10 mm. If a uniform grid were to be used to capture the entire dendritic growth, $O(10^6 - 10^7)$ grid points would be necessary in 2D and $O(10^9 - 10^{11})$ grid points would be necessary in 3D.

Solving the multiscale features with a uniformly fine computational mesh is therefore impractical and too computationally costly, while coarser uniform meshes would under-resolve the fine-scale features, leading to erroneous results. These considerations motivate the use of adaptive mesh refinement and coarsening methods, which allow for locally varying mesh size and thus can potentially save many orders of magnitude in the number of unknowns required for a given accuracy [38–40,51–53,76,78–93]. In this paper, we follow the approach of Min and Gibou, who introduced a node-based PDE solvers on non-graded quadtree data structures [51–53,76,79–88] and develop numerical methods for the simulation of solidification processes of binary alloys.

Referring to Fig. 2, the root of the quadtree initially represents the computational domain, which is then split into four equal size children according to the chosen refinement criteria. The level is defined to be zero for the root and incremented by one every time a new generation of children is introduced. Throughout the article we call a 'grid of level n' a quadtree of depth n, i.e., a grid for which the corresponding uniform grid with the same resolution has 4^n cells. A quadtree is non-graded if the difference of levels between adjacent cells is unconstrained.

4.1 The Approach of Min and Gibou

We follow the approach of Min and Gibou [51–53], who developed discretization formulas of general operators for node-sampled functions. The main difficulty in discretizing differential operator on quadtree grids is in defining valid values of the solution at T-junctions nodes, i.e. nodes that are missing a direct neighbor in one direction, as illustrated in Fig. 3. A third-order

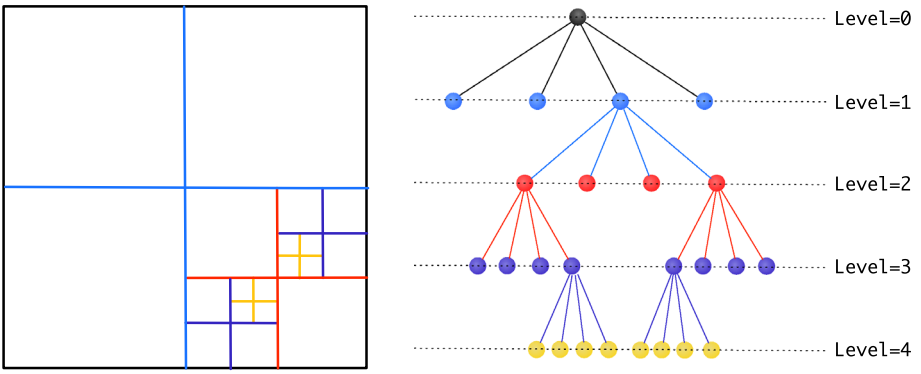

Fig. 2 Discretization of a two-dimensional domain (*left*) and its quadtree representation (*right*). The entire domain corresponds to the root of the tree (level 0). Each cell can then be recursively subdivided further into four children. In this example, the tree is non-graded, since the difference of level between some adjacent cells exceeds one

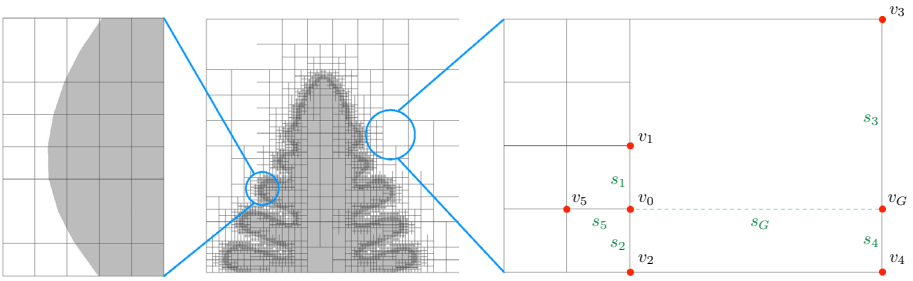

Fig. 3 Local grid configuration near a node v_0. The schematic on the right describes a T-junction where a node is missing in the x-direction. In contrast, the grid near the interface Γ is locally uniform (*left*) and therefore standard discretizations can be used

definition of a ghost node u_g^G can be defined at T-junctions:

$$u_g^G = \frac{u_3 s_4 + u_4 s_3}{s_3 + s_4} - \frac{s_3 s_4}{s_1 + s_2}\left(\frac{u_1 - u_0}{s_1} + \frac{u_2 - u_0}{s_2}\right),$$

which allows for the definition of standard approximations of derivatives in a dimension-by-dimension framework. For example, referring to Fig. 4, we use the central difference formulas for u_x and u_{xx}:

$$D_x^0 u_0 = \frac{u_2 - u_0}{s_2} \cdot \frac{s_1}{s_1 + s_2} + \frac{u_0 - u_1}{s_1} \cdot \frac{s_2}{s_1 + s_2}$$

and

$$D_{xx}^0 u_0 = \frac{u_2 - u_0}{s_2} \cdot \frac{2}{s_1 + s_2} - \frac{u_0 - u_1}{s_1} \cdot \frac{2}{s_1 + s_2}, \tag{8}$$

the forward and backward first-order accurate approximations of the first-order derivatives:

$$D_x^+ u_0 = \tfrac{u_2 - u_0}{s_2},$$
$$D_x^- u_0 = \tfrac{u_0 - u_1}{s_1},$$

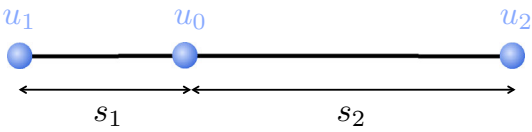

Fig. 4 A one-dimensional adaptive grid

and the second-order accurate approximations of the first-order derivatives:

$$D_x^+ u_0 = \frac{u_2 - u_0}{s_2} - \frac{s_2}{2}\text{minmod}\left(D_{xx}^0 u_0, D_{xx}^0 u_2\right),$$
$$D_x^- u_0 = \frac{u_0 - u_1}{s_1} + \frac{s_1}{2}\text{minmod}\left(D_{xx}^0 u_0, D_{xx}^0 u_1\right),$$

with the operator D_{xx}^0 defined in Eq. (8) and where the`minmod` slope limiter [94,95], defined as:

$$\text{minmod}(x, y) = \begin{cases} x & \text{if } |x| > |y|, \\ y & \text{otherwise,} \end{cases}$$

is used to avoid differencing across regions where gradients are large (i.e. near kinks). Similarly, approximations for first-order and second-order derivatives are obtained in the y-direction.

Although several refinement criteria could be defined, we are principally interested in automatically refining the mesh where the interface lies. Based on the work of Strain [96] and Min [97], Min and Gibou [51] proposed the following simple refinement criteria for generating such grids: Starting from a root cell split any cell C if:

$$\min_{v \in \text{vertices}(C)} |\phi(v)| \leq \text{Lip}(\phi) \cdot \text{diag-size}(C), \tag{9}$$

where diag-size(C) refers to the length of the diagonal of the current cell C and v refers to a vertex (node) of the current cell. Typical results are depicted in Fig. 3. We also note that it is straightforward to generate a grid with a uniform band around the interface.

Remark The refinement criteria used is dictated by the multiscale nature of the dendritic growth problem, i.e. small cells are used in a small band around the interface to capture the solute boundary layer and the grid is coarsen away from the solidification front. A consequence of this refinement is that the grid is uniform around the interface, which considerably eases the treatment of boundary conditions.

5 Sharp Numerical Approach for Simulating Multimaterial SuperAlloys

As mentioned in the introduction, we seek to develop a numerical method that approximates the sharp model for solidification of a binary alloy. The main focus is on (i) how to impose the boundary condition in a way that does not artificially smear the concentration profile across the solidification front and (ii) using efficient mesh refinement strategies to capture small length scales while reducing the computational burden. In this section, we first present the main steps of our solution process in **Algorithm** 1 before focusing on the details of the different numerical techniques.

Define all the parameters: m_L, k, λ, D_L, ρ, c, t_{initial}, t_{final}, , ϵ_C, ϵ_V
Initialize T^0, $C^{l,0}$, $C^{s,0}$, ϕ_0 and set $t = t_{\text{initial}}$
while $t < t_{final}$ **do**
  Compute V_Γ and time step Δt
  Advect ϕ^n to obtain ϕ^{n+1} using (6)
  reinitialize ϕ^{n+1} using (7)
  Remesh for the new interface ϕ^{n+1} using (9)
  Initialize $C^{l,n+1} = C^{l,n}$, $C^{s,n+1} = C^{s,n}$
  while $||V_\Gamma^p - V_\Gamma^{p-1}||/||V_\Gamma^p|| >$ Tol **do**
    Compute V_Γ from $C^{l,n+1}$, $C^{s,n+1}$ according to (5)
    Solve (1) for T^{n+1} with the jump conditions (4) and (2)
    Use T^{n+1} and (3) to compute the interfacial concentration
    Solve (1) for $C^{l,n+1}$, $C^{s,n+1}$
  end
  Update the quantities: $t = t + \Delta t$, $C^{l,n} = C^{l,n+1}$, $C^{s,n} = C^{s,n+1}$, $T^n = T^{n+1}$
end

Algorithm 1: General steps.

The convergence criteria $||V_\Gamma^{p+1} - V_\Gamma^p||/||V_\Gamma^p|| >$ Tol is based on the relative difference in the interface velocity V_Γ between two functional iterations, which we require to be under a certain tolerance Tol. We take the L^1-norm and consider only the nodes in a band of $4\triangle x$ around the interface. We take Tol $= 10^{-5}$ and note that the iterative method was found to converge to the same solution even for very small tolerance (10^{-8}). We note that other iterative processes could be considered in terms of ordering the variables update. We have observed that the proposed ordering produces convergent results, although no mathematical proofs are given in the present manuscript. The proof would make for interesting future work

5.1 Solving for the Concentration Fields

When solving for the concentration field, we seek to impose the boundary condition at the solid–liquid interface in a sharp fashion, namely the Gibbs–Thompson equation (3) and the solute rejection equation (5). We follow the approach of Chen et al. [76] and present here the main steps. The Gibbs–Thompson equation is a Dirichlet boundary condition on the moving solidification front Γ:

$$C^l\big|_\Gamma = \frac{T - T_m}{m_L} - \frac{\epsilon_c(\theta)}{m_L}\kappa - \frac{\epsilon_v}{m_L}V_\Gamma \qquad x \in \Gamma. \tag{10}$$

The concentration diffusion equation for the solid phase in (1) is discretized in time using a Crank-Nicholson scheme:

$$\left(I - \frac{D^l \triangle t}{2}\Delta_h^{n+1}\right) C^{l,n+1} = C^{l,n} + \frac{D^l \triangle t}{2}\Delta_h^n C^{l,n}, \qquad x \in \Omega^l, \tag{11}$$

where Δ_h^n and Δ_h^{n+1} are approximations of the Laplacian at time t^n and t^{n+1}, respectively. For grid nodes that are not adjacent to the interface, Eq. (8), and the similar approximation corresponding to the y-direction, are used to fill one row in the linear system described by Eq. (11) for $C^{l,n+1}$. For the nodes adjacent to the interface, the discretizations are modified to enforce the Dirichlet boundary condition (10): Consider the case depicted in Fig. 5, where the node v_1 is outside the irregular domain Ω^l. By enforcing a band of uniform cells along the interface, we guarantee that v_0 has a direct neighboring node in each direction. The

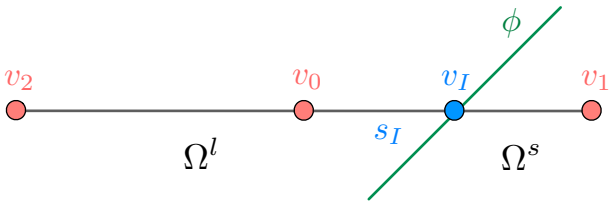

Fig. 5 Schematic representing the case where the solidification front crosses between the nodes v_0 and v_1 at the location v_I. We denote by s_n the distance between v_0 and v_n

discretization of $C^l_{xx}(v_0)$ is then given by:

$$\frac{\partial^2 C^l}{\partial x^2}(v_0) = \left(\frac{C^l_I - C^l_0}{s_I} - \frac{C^l_0 - C^l_2}{s_2} \right) \frac{2}{s_I + s_2} + O(\Delta x^2),$$

where $C^l_i = C^l(v_i)$, $C^l_I = C^l\big|_\Gamma$ is given by Eq. (10) and the distance s_I between v_0 and v_I is calculated from the level-set function. This discretization has been shown to provide second-order accurate approximation (in both L^1 and L^∞-norms) for both the solution of the diffusion equation with Dirichlet boundary condition on arbitrary domains and its gradient. Similarly, the solid concentration diffusion is discretized in the same way. We refer the interested reader to [76] for the detailed methodology.

5.2 Solving for the Temperature Field

The remaining interfacial conditions, i.e. the continuity of the temperature (2) and the heat flux balance (4). Combined with the diffusion equation this interfacial conditions define the following jump problem:

$$\begin{cases} \partial T/\partial t &= \lambda \Delta T, & \forall \boldsymbol{x} \in \Omega, \\ [T] &= 0, & \forall \boldsymbol{x} \in \Gamma, \\ [\partial T/\partial \boldsymbol{n}] &= (L/k) V_\Gamma, & \forall \boldsymbol{x} \in \Gamma. \end{cases} \tag{12}$$

As for the concentration field we start by discretizing the heat diffusion equation in (12) using a Crank–Nicholson scheme:

$$\left(I - \frac{\lambda \Delta t}{2} \Delta_h^{n+1} \right) T^{n+1} = T^n + \frac{\lambda \Delta t}{2} \Delta_h^n T^n, \qquad x \in \Omega.$$

For nodes that are not adjacent to the interface this above equation is easily discretized using formula (8) in the x-direction and similar one in the y-direction to build the corresponding row in the linear system for T^{n+1}. For nodes adjacent to the interface, we propose here a simple and robust method to enforce the jump conditions (4) and (2). The two main advantages of this method are that (*i*) the discretization stencil is compact, i.e. only nodes adjacent to the current node v_0 are used and (*ii*) the structure of the resulting discretization matrix is not affected; only the right-hand side is, which makes the implementation straightforward. In particular the positive definiteness of the matrix is preserved, which guarantee the convergence of iterative solvers.

A general configuration is depicted in Fig. 6, where the current node $v_0 \in \Omega^s$ has two neighbors, v_2 and v_4, both across the solidification front. Following ideas of the ghost-fluid method set forth in [98,99], we introduce ghost values, T^s_2 and T^s_4, for the temperature field

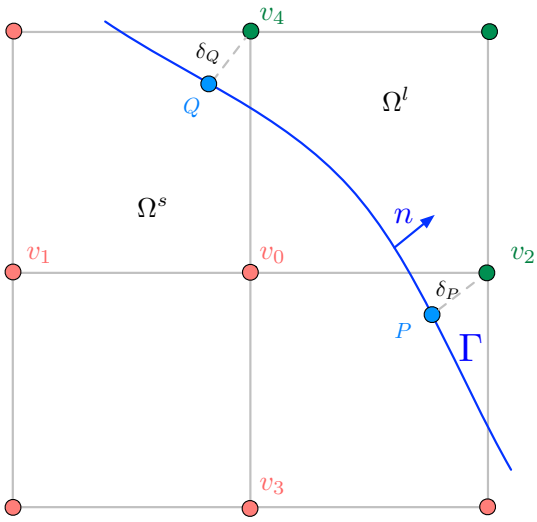

Fig. 6 Solving for the temperature field: grid configuration near the interface

in the solid phase at these two nodes. These fictitious values are related to the real values of the temperature field at the corresponding nodes through the jump conditions:

$$T_2^s = T_2^l + [T]_P + \delta_P \left[\frac{\partial T}{\partial \boldsymbol{n}}\right]_P + O\left(h^2\right),$$
$$T_4^s = T_4^l + [T]_Q + \delta_Q \left[\frac{\partial T}{\partial \boldsymbol{n}}\right]_Q + O\left(h^2\right),$$

where $h = \max(\Delta x, \Delta y)$, the points P and Q are the orthogonal projections of nodes v_2 and v_4 on the interface Γ and δ_P and δ_Q are the distances from P and Q to v_2 and v_4, respectively. Since the temperature is continuous across the interface, these equations simplify to:

$$T_2^s = T_2 + \delta_P \left[\frac{\partial T}{\partial \boldsymbol{n}}\right]_P + O\left(h^2\right), \tag{13}$$
$$T_4^s = T_4 + \delta_Q \left[\frac{\partial T}{\partial \boldsymbol{n}}\right]_Q + O\left(h^2\right). \tag{14}$$

The standard central difference approximation of the Laplacian operator at the node v_0, using the ghost nodes T_2^s and T_4^s reads:

$$\Delta_h T(v_0) = \frac{T_2^s - 2T_0 + T_1}{\Delta x^2} + \frac{T_4^s - 2T_0 + T_3}{\Delta y^2} + O\left(h^2\right).$$

Using Eqs. (13) and (14), this discretization is written as:

$$\Delta_h T(v_0) = \frac{T_2 - 2T_0 + T_1}{\Delta x^2} + \frac{T_4 - 2T_0 + T_3}{\Delta y^2} + \frac{\delta_P}{\Delta x^2}\left[\frac{\partial T}{\partial \boldsymbol{n}}\right]_P + \frac{\delta_Q}{\Delta y^2}\left[\frac{\partial T}{\partial \boldsymbol{n}}\right]_Q + O\left(h^2\right),$$

or,

$$\Delta_h T(v_0) = \widetilde{\Delta_h T_0} + \frac{\delta_P}{\Delta x^2}\left[\frac{\partial T}{\partial \boldsymbol{n}}\right]_P + \frac{\delta_Q}{\Delta y^2}\left[\frac{\partial T}{\partial \boldsymbol{n}}\right]_Q + O\left(h^2\right),$$

where $\widetilde{\Delta T_0}$ is the standard central difference discretization of the Laplacian operator. It is clear that the only difference with the discretization of a standard Laplace equation is seen on the right-hand side of the linear system; the matrix itself is unchanged. Note that this approach is different from the ghost-fluid treatment of [99] that considers the jump in the Cartesian direction only.

Remark We note that this approach is only valid in the case where there is no jump in the diffusivity coefficient, which is the case in this problem. In the more general case where the diffusivity coefficient λ is different in each phase, we refer the interested reader to the method presented in [100] and the references therein.

5.3 Interface Velocity Calculation

The calculation of the interface velocity V_Γ follows from Eq. (5):

$$V_\Gamma = -\frac{D_L}{(1-k_p)C^l}\frac{\partial C^l}{\partial \boldsymbol{n}}\bigg|_\Gamma,$$

and is calculated in three steps. First the solute concentration C^l, is extended to the entire domain using a third-order extrapolation procedure described in [51,101]. The concentration gradient at every node is then computed using standard central differencing and then used to compute the velocity everywhere according to the above equation. Finally the velocity field is extrapolated in a constant fashion in a small band around the interface in the normal direction as originally suggested by [70,102].

5.4 Time Step Definition

Once the interface velocity is known, the level-set function is advected using the second-order accurate semi-Lagrangian method on quadtree of [51]. This method is unconditionally stable, therefore does not introduce any time step restriction. Since the Crank–Nicholson scheme used to discretize the temperature and concentration diffusion equations are also unconditionally stable, the time step restriction of the present algorithm is dictated by accuracy concerns only. We take a time step that accounts for the maximum interface speed, i.e. prevents the interface to move by more than $\alpha\triangle x$:

$$\triangle t = \alpha\frac{\triangle x}{V_{\max}},$$

where $\triangle x$ is the size of the smallest grid cell and $V_{\max}$ is the maximum value of the interface normal velocity. In addition, in order to capture interesting developing features such as the growth of dendrite secondary arms, we further consider a time step of

$$\triangle t \leq \frac{1}{\max\left(|\kappa V_\Gamma|\right)},$$

where $\max\left(|\kappa V_\Gamma|\right)$ the maximum value of the product of the interface's curvature times the normal velocity. This condition allows the scheme to capture features of the order of $1/\kappa$, the smallest length scale resolved by the grid. The time step we take is therefore:

$$\triangle t = \min\left(\alpha\frac{\triangle x}{V_{\max}}, \frac{1}{\max\left(|\kappa V_\Gamma|\right)}\right)$$

The parameter α is typically set to be.5.

5.5 Computational Efficiency

The use of quadtree adaptive grids significantly reduces the number of degrees of freedoms, which contributes to efficient computation. In addition, the linear system is solved by the multigrid method on quadtree grids of Theillard et al. [103]. This method, like it is standard with multigrid methods [104], scales linearly with the number of nodes [103]. Since the other procedures used in this algorithm exhibit the same scalability, the overall method scales linearly with the number of nodes. We have parallelized the implementation on a shared memory architecture using the openMP library.

Remark The level-set function is reinitialized using the algorithm presented in [51], where the fictitious time step is proportional to the size of the local cell. Typically, we use only five iterations to produce an accurate distance function close to the interface. In addition, we note that increasing the number of iterations does not have any influence on the accuracy of the method.

6 Numerical Experiments: Solidification of an Ni–Cu Alloy

In this section we apply the method previously described to the solidification of a Ni–Cu alloy in two spatial dimensions. This system is selected since it has been well-characterized experimentally. The computational domain is a square box of size l and solidification is triggered by imposing a negative heat gradient G from top to bottom and a cooling rate V, as illustrated in Fig. 7. Figure 8 illustrates a typical result of the simulation of a binary alloy. Figure 8(a) presents the dendrite shape, the temperature distribution (red–blue scale) and the solute concentration (gray scale). This simulation corresponds to the regime of dendritic growth where primary and secondary arms are present. Figure 8(b) depicts the quadtree grid for which the highest resolution is automatically enforced in a small band around the interface, while leaving regions with a slow varying solution at a much coarser resolution. The width of the band is defined as to capture the solute's boundary layer. The concentration profile is also seen in Fig. 8c to be *sharp*, i.e. the concentration jumps across the solidification front, faithfully approximating the physical model. The important process of solute rejection is clearly captured by the simulation. We note that the diffusion coefficient in the solid phase is several orders of magnitude smaller than that in the liquid phase. Therefore, similar results are obtained whether or not the solution of the concentration field is computed in the solid phase. In what follows, we have simply ignored the concentration's diffusion in the solid phase, noting that the method presented allows for the concentration in both the solid and liquid phases to be computed.

We start by providing numerical evidence on the convergence of our method by studying the interface velocity and the global energy. We then show that our approach is able to simulate a number of known physical properties, such as the release of latent heat as well as the primary and secondary arm spacing. In the case of unstable growth, no forced numerical perturbations are introduced; rather the observed instability and subsequent dendrites are triggered by the numerical truncation errors only. A typical computation in a domain containing between 10 and 20 dendrites on a level 10 quadtree takes a few hours on an iMac 3.4 GHz with eight processors. Increasing the resolution by one level increases the computational time by four, i.e. slightly less than a day.

The parameters of the problems are the melting temperature $T_m = 1,728\,\mathrm{K}$, the liquidus slope $m_L = 357\,\mathrm{K/at.\,frac.}$, the partition coefficient $k_p = 0.86$, the initial concentration $C_0 = 0.40831$ at. frac., the latent heat $L = 2350\,\mathrm{J/cm^3}$, the curvature undercooling coef-

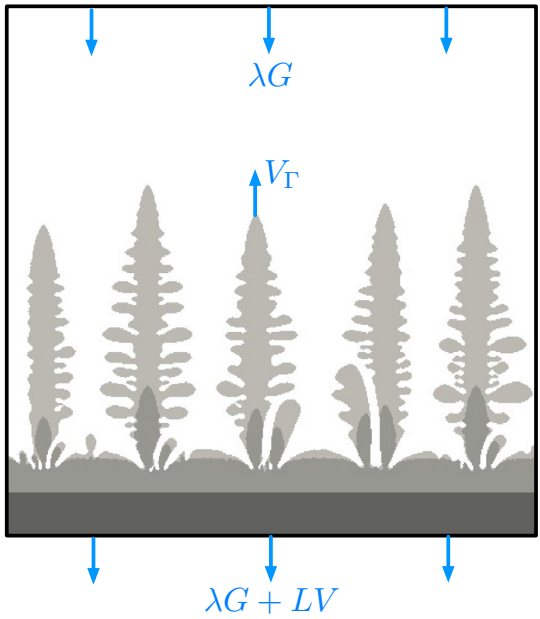

Fig. 7 Problem setup: the initial planar interface (represented in *dark grey*) is progressively cooled down by imposing a heat gradient G and a cooling rate V, which are implicitly enforced through the *top* and *bottom* wall boundary conditions. In the case where the interface is unstable, small perturbations first appear (*grey interface*) and grow into larger dendritic structures (*light grey*). The *right* and *left* walls are considered fully insulated, i.e. the normal gradient of the solute concentration on all the wall is considered to be zero (Neumann boundary condition). In this schematics, V_Γ refers to the velocity at the dendrites' tips

ficient $\epsilon_c = 2.7207 \times 10^{-5}\,\mathrm{cm\,K}$, the kinetic undercooling $\epsilon_V = 2.27 \times 10^{-2}\,\mathrm{s\,cm^{-1}\,K}$, the anisotropy coefficient $\epsilon = 0.05$, the heat diffusivity $\lambda = 1.486 \times 10^{-1}\,\mathrm{cm^2/s}$, the density $\rho = 8.88 \times 10^{-3}\,\mathrm{kg/cm^3}$, the specific heat $c = 4.6 \times 10^2\,\mathrm{J/kg\,K}$, the heat diffusivity $k = 6.07 \times 10^{-1}\,\mathrm{W/cm\,K}$ and the solute diffusion constant $D_l = 10^{-5}\ \mathrm{cm^2/s}$ [50].

6.1 Stable Planar Interface

In this section we consider the simplest solidification regime, i.e. that of a stable planar solidification front. The relative simplicity of this case allows us to compare our numerical results to theoretical predictions and illustrate the convergence of our method.

6.1.1 Convergence Analysis

We set the thermal gradient $G = 2.15 \times 10^4$ K/cm, the length computational domain $l = .05$ mm and we select a cooling velocity V such that the initial planar interface remains planar along the solidification process. According to the Mullins–Sekerka analysis [105], a sufficient condition for this regime to be reached is for the interfacial velocity V_Γ to be outside of the range $[10^{-2}, 10^{-3}\,\mathrm{cm/s}]$. The interfacial velocity cannot be directly imposed but can be controlled through the cooling velocity V. In the general case of dendritic growth, no explicit expression relates those two quantities, and we can only show that in cases where a planar interface is stable, the relation $V_\Gamma < V$ holds. Therefore by selecting $V = 0.01\,\mathrm{cm/s}$, we ensure that the interface velocity will remains stable. The resulting simulated planar solidification front is depicted on Fig. 9 at $t = .1$. Note that the value we took for the interface's velocity is close to the boundary of the Mullins–Sekerka's loop. The fact that the simulation produces a stable interface growth illustrates part of the robustness of the approach.

We start our analysis by looking at the evolution of the interface's velocity as the mesh resolution increases. Figure 10a clearly illustrates the convergence of the method as the grid is

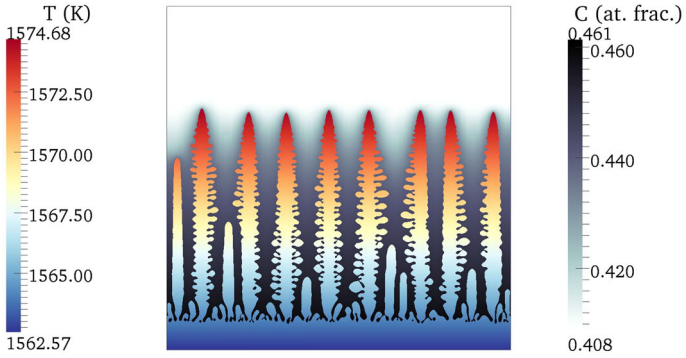

(a) Temperature distribution.

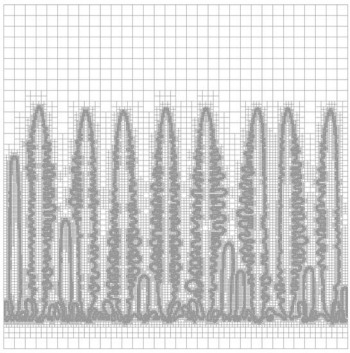

(b) Adaptive quadtree mesh.

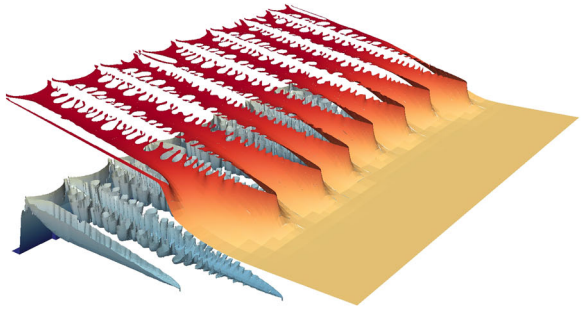

(c) Concentration field that is clearly discontinuous across the solidification front, faithfully approximating the *sharp* macroscopic model.

Fig. 8 Typical simulation of a binary alloy growth using our sharp interface simulation engine (Color figure online)

refined: initially the solute is equal to a constant C_0, therefore the interface's velocity, defined through the solute rejection equation (5), is initially zero before progressively increasing until it reaches its asymptotic value. We also note that, as expected, the interface's velocity is always smaller than the cooling velocity, i.e. $V_\Gamma < V$. In the asymptotic regime, under the assumption that $kG >> LV$ (in this example $(kG)/(LV) = 5.553 \times 10^2$), a simple power

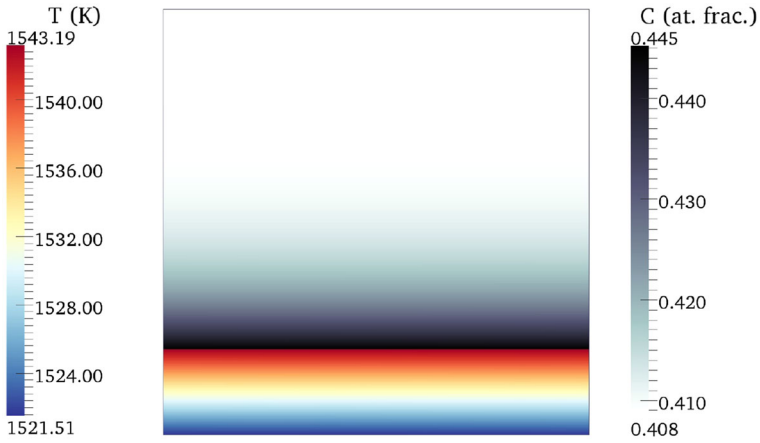

Fig. 9 Temperature field inside the solid phase (*blue–red color scheme*) and solute concentration field (*grey scheme*) in the case of a planar interface (Color figure online)

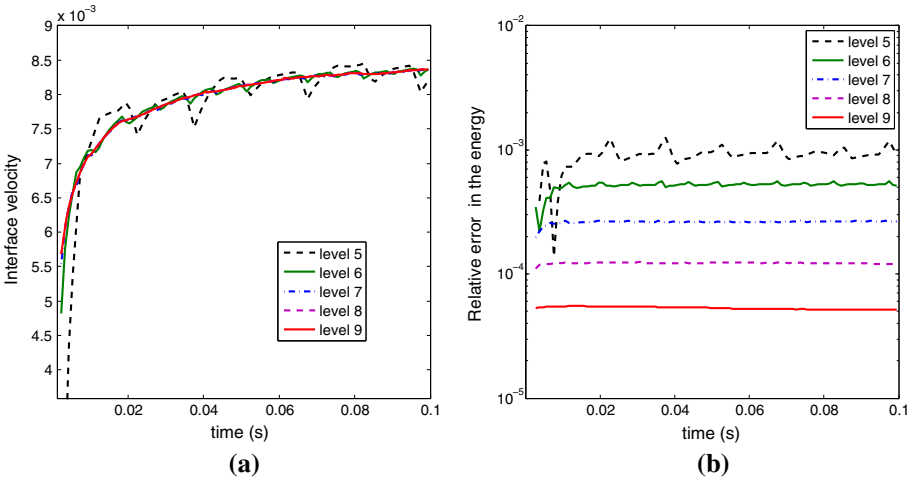

(a) **(b)**

Fig. 10 Convergence (**a**) and accuracy (**b**) under grid refinement of our numerical method in the case of stable planar interface

balance of the entire system gives us:

$$LV = LV_\Gamma + \frac{\rho c l}{L} G.$$

The left-hand-side term accounts for the heat flux pumped out of the computational domain, while the right hand side terms account for the release of latent heat and the energy loss due to the conductivity, respectively. From this equation we get that

$$V_\Gamma = \frac{V}{1 + \frac{\rho c l G}{L}}. \tag{15}$$

Applying the above formula for the current parameters we find that $V_\Gamma = 8.425 \times 10^{-3}$ cm/s, which is extremely close to the numerical asymptotical value $V_\Gamma = 8.385 \times 10^{-3}$ cm/s.

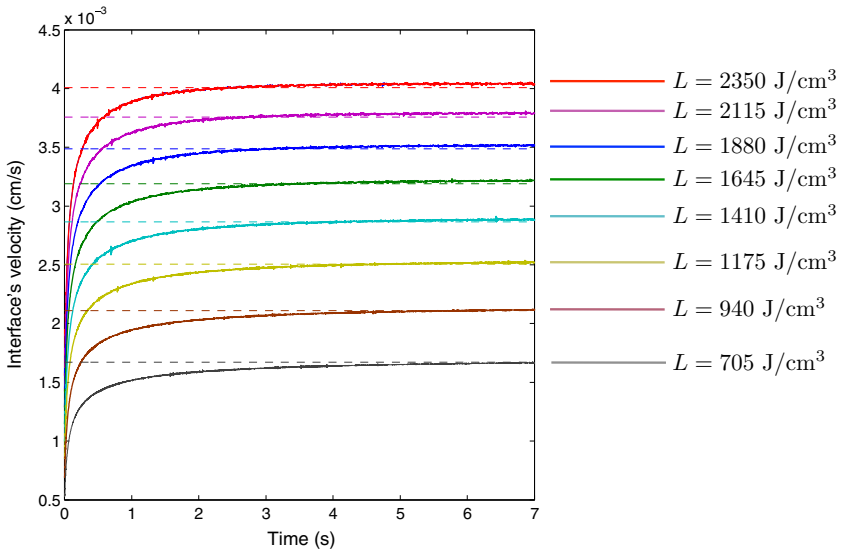

Fig. 11 Interface velocity profile (*solid lines*) for different values of the latent heat. The theoretical asymptotic values are represented by the *dash lines*

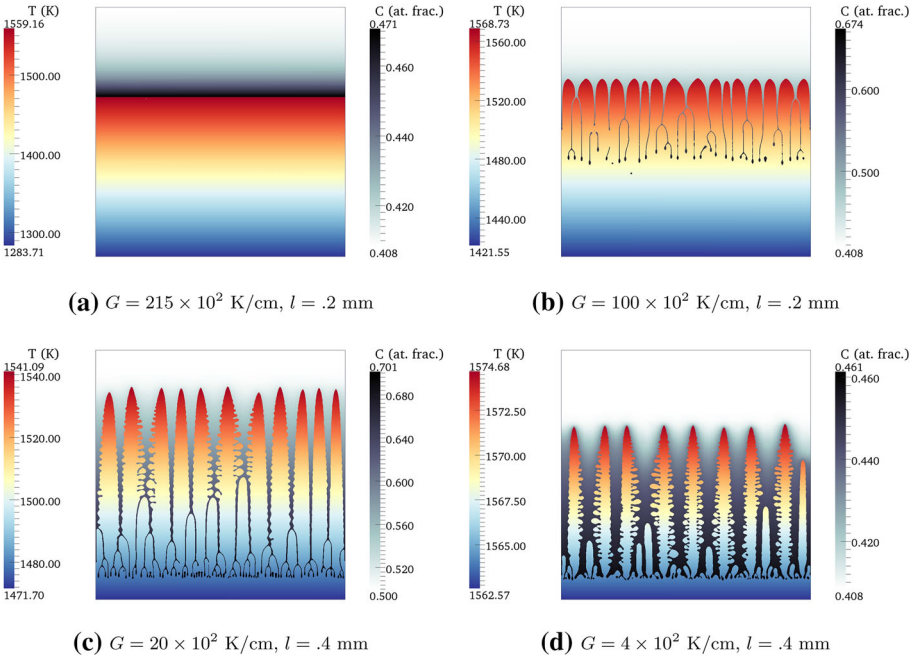

Fig. 12 Planar-Cellular-Dendritic transition. In this example the cooling velocity V is set to 0.01 cm/s. Starting from the stable configuration (**a**) we progressively increase the imposed heat gradient G and successively observe the planar-cellular (**b**) and cellular-dendritic transition (**c**, **d**). For G=2 × 10^3 K/cm (**c**), both the cellular and dendritic formations are observed

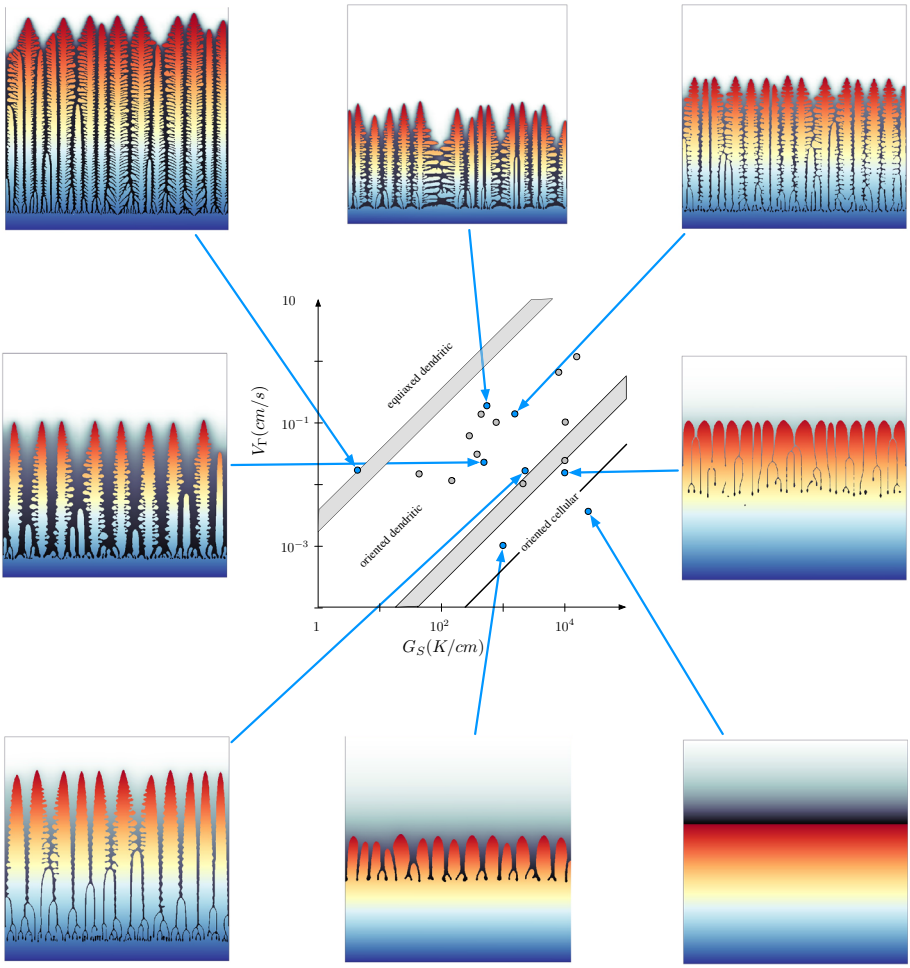

Fig. 13 Resulting crystalline configuration for different values of the cooling parameters. The *blue dots* represent the result for which the obtained geometry is depicted, while the *grey dots* represent numerical scenarios that had been numerically observed but that are not represented. Both are indexed according to the measured interface velocity and thermal gradient in the solid phase. The diagram represented in the *center*, and to which our result are compared, was originally presented in [106] (Color figure online)

We now consider the total energy of the system, $E(t)$, which is given by:

$$E(t) = L \int_{\Omega^l} ds + \rho c \int_{\Omega} T(x, y, t) ds, \tag{16}$$

to study the accuracy of the method. This can be expressed in the present case as (cf. Appendix B):

$$E(t) = LVht + E(0). \tag{17}$$

Using Eqs. (16) and (17) we can numerically compute the total energy and compare it to its theoretical value. The resulting relative error as a function of time and grid refinement level

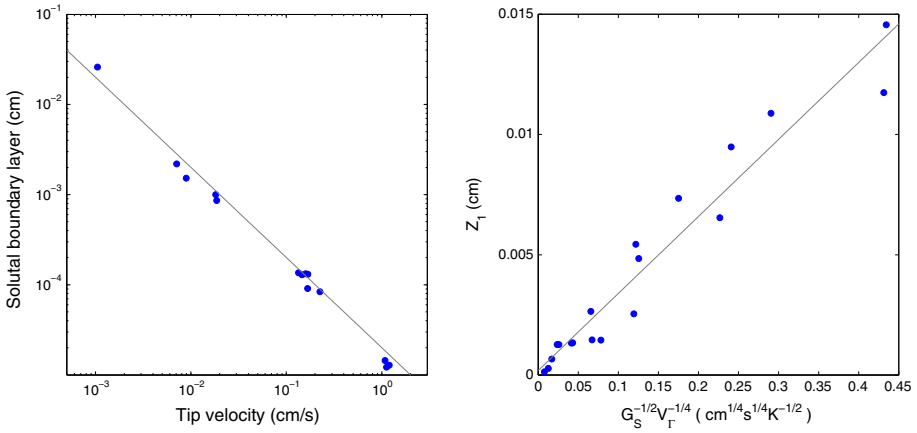

Fig. 14 **a** Numerical solutal boundary layer as a function of the tip velocity. The *solid line* represents the theoretical value. **b** Primary spacing as a function of the tip velocity and the temperature gradient in the solid phase. The slope of the best fit line was found to be .0307

is given in Fig. 10b. This example shows the strong connection between the level of the grid and the decrease in the relative error.

6.1.2 Impact of the Latent Heat

In this section we study the impact of the latent heat on the interface's velocity given by the approximation (15). To do so we reproduce the calculations performed in the previous section on a larger computational domain (l=.4 mm) and progressively vary the latent heat from its original value (2,350 J/cm^3) by decrements of 235 J/cm^3. The calculations are performed for a maximum resolution of 4, 096 and a minimal resolution of 32. We note that by decreasing the value of the latent heat, the condition $kG >> LV$ is still satisfied and therefore the approximation (15) still holds. As illustrated in Fig. 11, for all the values of the latent heat, the numerical and theoretical asymptotic values agree well. In fact the highest relative error is 1.366×10^{-2} and occurred in the case where the latent heat is 2,115 J/cm^3. This confirms that the latent heat is properly released.

6.2 Planar-Cellular-Dendritic Transitions

Starting from the previous stable configuration ($G = 2.15 \times 10^4$ K/cm and $V = 0.01$ cm/s) we progressively decrease the imposed thermal gradient. We respectively take for the minimum and maximum resolution 32 and 2,048. By doing so we observe the planar to cellular and cellular to dendritic transitions depicted in Fig. 12. Figure 13 represents the resulting crystal structures for a wider spectrum of the cooling parameters G and V. These results match extremely well with the predictions (based on experimental observations) of [106]. To our knowledge, our results show for the first time that it is possible to generate these maps with a fully computational approach.

6.2.1 Solutal Boundary Layer

For each simulation depicted in Fig. 13 the tip's velocity and the solutal boundary layer are measured and reported on Fig. 14a. The solutal boundary was defined as the distance

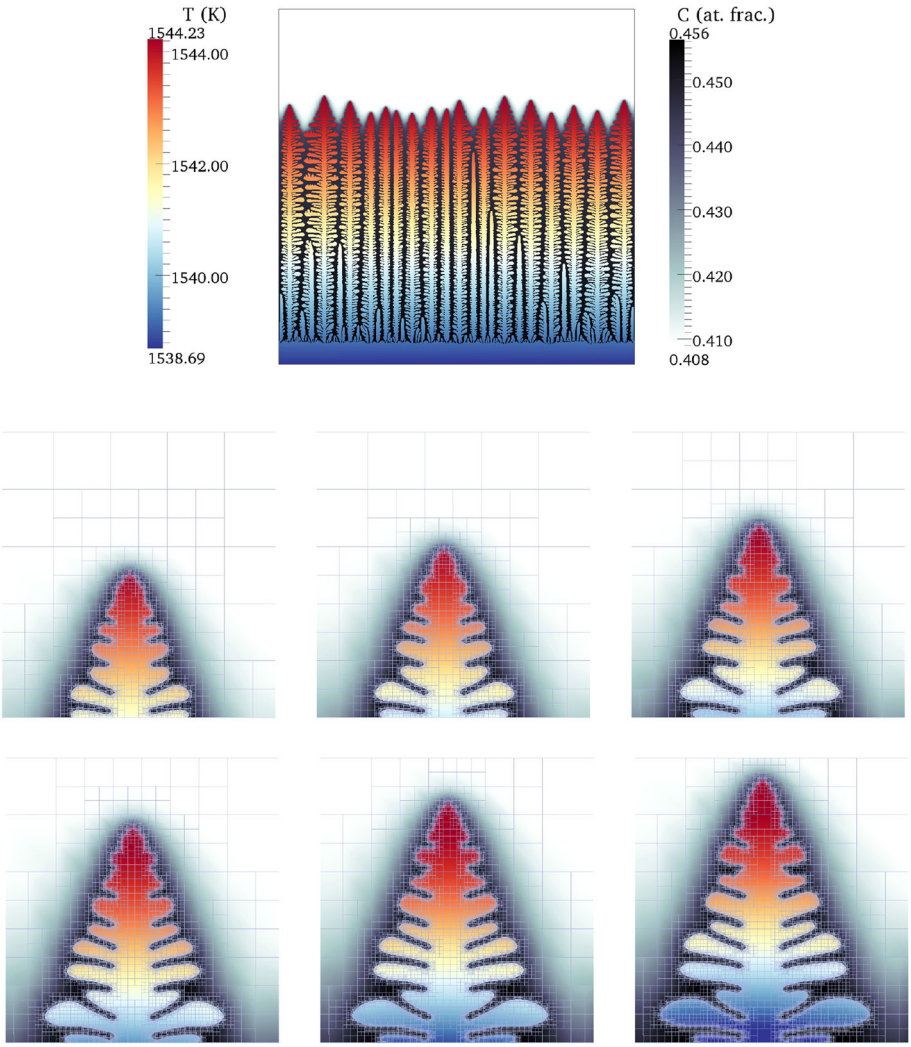

Fig. 15 Development of the secondary arms. *Top* entire simulation. *Bottom* zoom on the tip of a dendrites a different time step

(in the normal direction to the interface direction) between the tip and the point where the concentration drops to 5 % away from its asymptotic value C_0. The boundary layers obtained from the simulations are close to the theoretical values $\delta_S = 2D^l / V_\Gamma$.

6.2.2 Primary and Secondary Arms Spacing

The most common formula used for the primary arm spacing Z_1 as a function of the heat gradient and the tip velocity, is of the form:

$$Z_1 = AG_S^{-n} V_\Gamma^{-m}, \tag{18}$$

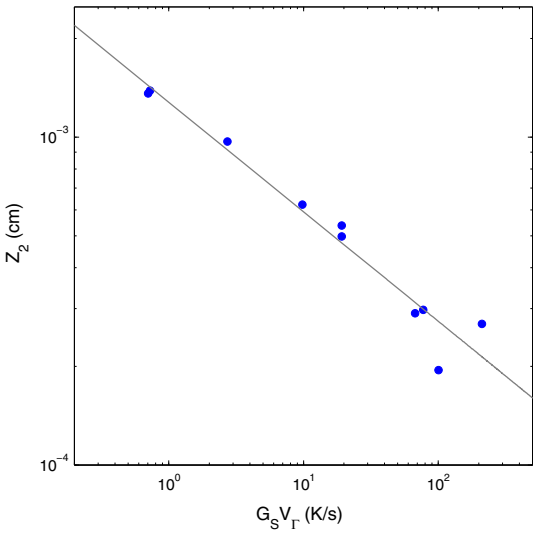

Fig. 16 Secondary arms spacing as a function of the tip velocity and the temperature gradient in the solid phase in a log–log scale

where $n = 1/2$ and $m = 1/4$. Here we only focus on the results that exhibit primary arms and measure the average primary spacing along with the tip velocity and the heat gradient in the solid phase. The results presented on Fig. 14b show that our numerical results match well the predictions of Eq. (18). The coefficient A is found to be $\sim 0.0307\,\mathrm{cm}^{3/4}\mathrm{s}^{-1/4}\mathrm{K}^{1/2}$. We also perform a linear regression of $\log(Z_1)$ as a function of $\log(G_S^{-1/2} V_\Gamma^{-1/4})$ and find that the slope of the best fit line is 1.0453, which is close to the expected value of 1. The constant coefficient in the linear regression, which is expected to be equal to 0, is found to be $\sim 1.087 \times 10^{-6}$.

We now focus on the development and spacing of secondary arms. Their formation is illustrated in Fig. 15. The calculations were performed with the following parameters: $V = 0.01$ cm/s, $G = 1$ K/cm and a computational domain of 0.3 cm. The minimum and maximum resolutions are respectively 32 and 4,096.

As for the primary spacing Z_1, no exact formula for the secondary spacing Z_2 as a function of G_S and V_Γ is universally accepted. However the most commonly used one states that Z_2 is a linear function of $\left(G_S V_\Gamma\right)^{-1/3}$:

$$Z_2 = B \left(G_S V_\Gamma\right)^{-1/3}, \tag{19}$$

where B is a constant coefficient that is specific to the alloy. As for the primary spacing analysis, the average secondary spacing was measured for the numerical cases that present secondary arms and then plotted in Fig. 16 as a function of $\left(G_S V_\Gamma\right)^{-1/3}$ and compared to the analytical expression (19). The numerical results agree well with the predictions. In particular a linear regression of $\log(Z_2)$ as a function of $\left(G_S V_\Gamma\right)$ has a slope of ~ -0.334, which is close to the expected value of $-1/3$.

7 Conclusion

We have developed a new numerical method for the modeling of the dendritic growth where the interface conditions are imposed in a sharp manner, ensuring that the physical properties

are properly captured. By using adaptive quadtree grids we were able to handle the inherent highly multiscale nature of this phenomena. This approach allowed us to produce numerical results that exhibit an excellent agreement with theoretical results. In addition, we have shown that this method can reproduce a wide range of growth, from planar to cellular to dendritic. In addition, we have shown that solidification mechanism maps predicting growth regimes as a function of thermal gradients and front velocities can be obtained with this approach.

Acknowledgments We would like to thank Dr. Jonathan Miller for stimulating discussions at UCSB and AFRL about solidification of binary alloys. We also thank Christopher Harrel for running some simulations while interning in the Computational Applied Science Laboratory as part of the CNSI INSET program at UCSB. The research of M. Theillard and F. Gibou was supported in part by ONR N00014-11-1-0027, NSF CHE 1027817 and by the W.M. Keck Foundation. In addition M. Theillard acknowledges support from a Dean's fellowship at UCSB. T. Pollock was supported in part by NSF DMREF Grant DMR 1233704.

References

1. Rogich, D., Matos, G.: The global flows of metals and minerals. In: Technical Report 1355, USGS Open File Report, Reston, VA (2008)
2. Seth, B.B.: Superalloys: the utility gas turbine perspective. In: Pollock, T.M., Kissinger, R.D., Bowman, R.R., et al. (eds.) Superalloys 2000, pp. 3–16. The Minerals, Metals and Materials Society (TMS), Warrendale, PA (2000)
3. Schafrik, R., Sprague, R.: Gas turbine materials. Adv. Mater. Process. **5**, 29–34 (2004)
4. Pollock, T., Tin, S.: Nickel-based superalloys for advanced turbine engines: chemistry, microstructure and properties. AIAA J. Propuls. Power **22**, 361–374 (2006)
5. Reed, R.C.: The Superalloys: Fundamentals and Applications. Cambridge University Press, Cambridge (2006)
6. Elliott, A., Pollock, T., Tin, S., King, W., Huang, S.-C., Gigliotti, M.: Directional solidification of large superalloy castings with radiation and liquid-metal cooling: a comparative assessment. Metall. Mater. Trans. A **35**, 3221–3231 (2004)
7. Brundidge, C., Miller, J., Pollock, T.: Development of dendritic structure in the liquid-metal cooled directional solidification process. Metall. Mater. Trans. **42A**, 2723–2732 (2011)
8. Brundidge, C., Pollock, T.: Processing to fatigue properties: benefits of high gradient casting for single crystal airfoils. In: Superalloys 2012, Proceedings 12th International Conference on Superalloys, TMS (2012)
9. Madison, J., Spowart, J., Rowenhorst, D., Aagesen, L., Thornton, K., Pollock, T.: Modeling fluid flow in three-dimensional single crystal dendritic structures. Acta Mater. **58**, 2864–2875 (2010)
10. Madison, J., Spowart, J., Rowenhorst, D., Aagesen, L., Thornton, K., Pollock, T.: Fluid flow and defect formation in the 3-dimensional dendritic structure of nickel-base single crystals. Metall. Mater. Trans. **43A**, 369 (2012)
11. Davis, S.: Theory of Solidification. Cambridge University Press, Cambridge (2001)
12. Zhu, M., Stefanescu, D.: Virtual front tracking model for the quantitative modeling of dendritic growth in solidification of alloys. Acta Mater. **55**(5), 1741–1755 (2007)
13. McFadden, G.B., Coriell, S.R., Sekerka, R.F.: Effect of surface free energy anisotropy on dendrite tip shape. Acta Mater. **48**(12), 3177–3181 (2000)
14. Kurz, W.: Dendritic growth. Int. Mater. Rev. **39**(26), 49–74 (1994)
15. Meiron, D.: Selection of steady-states in the two-dimensional symmetric model of dendritic growth. Phys. Rev. A. **33**, 2704 (1986)
16. Ben Amar, M., Pelcé, P.: Impurity effect on dendritic growth. Phys. Rev. A **39**(8), 4263–4269 (1989)
17. Langer, J.S.: Models of pattern formation in first-order phase transitions. In: Grinstein, G., Mazenko, G. (eds.) Directions in Condensed Matter Physics, p. 165. World Scientific, Singapore (1986)
18. Karma, A., Rappel, W.-J.: Quantitative phase-field modeling of dendritic growth in two and three dimensions. Phys. Rev. E **57**, 4323–4349 (1997)
19. Karma, A.: Phase-field formulation for quantitative modeling of alloy solidification. Phys. Rev. Lett. **87**, 115701 (2001)
20. Nestler, B., Danilov, D., Galenko, P.: Crystal growth of pure substances: phase-field simulations in comparison with analytical and experimental results. J. Comput. Phys. **207**, 221–239 (2005)

21. Schmidt, A.: Computation of three dimensional dendrites with finite elements. J. Comput. Phys. **125**, 293–312 (1996)
22. Karma, A., Rappel, W.J.: Phase-field modeling method for computationally efficient modeling of solidification with arbitrary interface kinetics. Phys. Rev. E **53**, R3017–R3020 (1996)
23. Echebarria, B., Folch, R., Karma, A., Plapp, M.: Quantitative phase-field model of alloy solidification. Phys. Rev. E **70**, 061604 (2004)
24. Pons, A.J., Karma, A., Akamatsu, S., Newey, M., Pomerance, A., Singer, H., Losert, W.: Feedback control of unstable cellular solidification fronts. Phys. Rev. E **75**, 021602 (2007)
25. Asta, M., Beckermann, C., Karma, A., Kurz, W., Napolitano, R., Plapp, M., Purdy, G., Rappaz, M., Trivedi, R.: Solidification microstructures and solid-state parallels: recent developments, future directions. Acta Mater. **57**, 941–971 (2009)
26. Gurevich, S., Karma, A., Plapp, M., Trivedi, R.: Phase-field study of three-dimensional steady-state growth shapes in directional solidification. Phys. Rev. E **81**, 011603 (2010)
27. Kopczynski, P., Rappel, W.-J., Karma, A.: Critical role of crystalline anisotropy in the stability of cellular array structures in directional solidification. Phys. Rev. Lett. **77**, 3387–3390 (1996)
28. Hurle, D.T.: Handbook of Crystal Growth. North Holland (1993)
29. Elder, K., Grant, M., Provatas, N., Kosterlitz, J.: Sharp interface limits of phase-field models. SIAM J. Appl. Math. **64**, 21604 (2001)
30. Boettinger, W.J., Warren, J.A., Beckermann, C., Karma, A.: Phase-field simulations of solidification. Ann. Rev. Mater. Res. **32**, 163–194 (2002)
31. Chen, L.-Q.: Phase-field models for microstructure evolution. Ann. Rev. Mater. Res. **32**, 113–40 (2002)
32. George, W.L., Warren, J.A.: A parallel 3d dendritic growth simulator using the phase-field method. J. Comput. Phys. **177**(2), 264–283 (2002)
33. Stinner, B., Nestler, B., Garcke, H.: A diffuse interface model for alloys with multiple components and phases. SIAM J. Appl. Math. **64**, 775–799 (2004)
34. Dorr, M., Fattebert, J.-L., Wickett, M., Belak, J., Turchi, P.: A numerical algorithm for the solution of a phase-field model of polycrystalline materials. J. Comput. Phys. **229**(3), 626–641 (2010)
35. Karagadde, S., Bhattacharya, A., Tomar, G., Dutta, P.: A coupled VOF-IBM-enthalpy approach for modeling motion and growth of equiaxed dendrites in a solidifying melt. J. Comput. Phys. **231**(10), 3987–4000 (2012)
36. Jeong, J.-H., Goldenfeld, N., Dantzig, J.: Phase field model for three-dimensional dendritic growth with fluid flow. Phys. Rev. E **64**, 41602 (2001)
37. Tryggvason, G., Bunner, B., Esmaeeli, A., Juric, D., Al-Rawahi, N., Tauber, W., Han, J., Nas, S., Jan, Y.-J.: A front-tracking method for the computations of multiphase flow. J. Comput. Phys. **169**, 708–759 (2001)
38. Heinrich, J., Zhao, P.: Front tracking finite element method for dendritic solidification. J. Comput. Phys. **173**, 765–796 (2001)
39. Zhao, P., Vénere, M., Heinrich, J., Poirier, D.: Modeling dendritic growth of a binary alloy. J. Comput. Phys. **188**(2), 434–461 (2003)
40. Singh, R., Shyy, W.: Three-dimensional adaptive cartesian grid method with conservative interface restructuring and reconstruction. J. Comput. Phys. **224**(1), 150–167 (2007)
41. Al-Rawahi, N.: Numerical simulation of dendritic solidification with convection: two-dimensional geometry. J. Comput. Phys. **180**(2), 471–496 (2002)
42. Eck, C., Knabner, P., Korotov, S.: A two-scale method for the computation of solid–liquid phase transitions with dendritic microstructure. J. Comput. Phys. **178**(1), 58–80 (2002)
43. Möller, P., Hansbo, P.: On advancing front mesh generation in three dimensions. Int. J. Num. Methods Eng. **38**, 3551–3569 (1995)
44. Fedoseyev, A.I., Alexander, J.D.: An inverse finite element method for pure and binary solidification problems. J. Comput. Phys. **130**(2), 243–255 (1997)
45. Skeldon, A., Cliffe, K., Riley, D.: Grid design for the computation of a hexagon-roll interaction using a finite element method. J. Comput. Phys. **133**(1), 18–26 (1997)
46. Bars, M.L., Worster, M.G.: Solidification of a binary alloy: Finite-element, single-domain simulation and new benchmark solutions. J. Comput. Phys. **216**(1), 247–263 (2006)
47. Zabaras, N., Ganapathysubramanian, B., Tan, L.: Modelling dendritic solidification with melt convection using the extended finite element method. J. Comput. Phys. **218**(1), 200–227 (2006)
48. Tan, L., Zabaras, N.: A level set simulation of dendritic solidification of multi-component alloys. J. Comput. Phys. **221**(1), 9–40 (2007)
49. Tan, L., Zabaras, N.: Modeling the growth and interaction of multiple dendrites in solidification using a level set method. J. Comput. Phys. **226**(1), 131–155 (2007)

50. Tan, L., Zabaras, N.: Multiscale modeling of alloy solidification using a database approach. J. Comput. Phys. **227**(1), 728–754 (2007)
51. Min, C., Gibou, F.: A second order accurate level set method on non-graded adaptive Cartesian grids. J. Comput. Phys. **225**(1), 300–321 (2007)
52. Chen, H., Min, C., Gibou, F.: A numerical scheme for the Stefan problem on adaptive Cartesian grids with supralinear convergence rate. J. Comput. Phys. **228**(16), 5803–5818 (2009)
53. Chen, H., Min, C., Gibou, F.: A second-order accurate FDM for the heat equation on irregular domains and adaptive grids. In: Proceedings of the Materials Research Society Symposium, San Francisco, CA, USA, vol. 910, pp. 907–910 (2006)
54. Benson, D.: Computational methods in Lagrangian and Eulerian hydrocodes. Comput. Methods Appl. Mech. Eng. **99**, 235–394 (1992)
55. Benson, D.: Volume of fluid interface reconstruction methods for multimaterial problems. Appl. Mech. Rev. **52**, 151–165 (2002)
56. DeBar, R.: Fundamentals of the KRAKEN code. Technical Report, Lawrence Livermore National Laboratory (UCID-17366) (1974)
57. Noh, W., Woodward, P.: SLIC (simple line interface calculation). In: 5th International Conference on Numerical Methods in Fluid Dynamics, 1976, pp. 330–340 (1976)
58. Youngs, D.: An interface tracking method for a 3D Eulerian hydrodynamics code. Technical Report, AWRE (44/92/35) (1984)
59. Dyadechko, V., Shashkov, M.: Moment-of-fluid interface reconstruction. Technical Report, Los Alamos National Laboratory (LA-UR-05-7571) (2006)
60. Popinet, S.: An accurate adaptive solver for surface-tension-driven interfacial flows. J. Comput. Phys. **228**(16), 5838–5866 (2009)
61. Glimm, J., Grove, J.W., Li, X.L., Zhao, N.: Simple front tracking. Contemp. Math. **238**, 133–149 (1999)
62. Juric, D.: A front-tracking method for dendritic solidification. J. Comput. Phys. **123**(1), 127–148 (1996)
63. Juric, D., Tryggvason, G.: Computations of boiling flows. Int. J. Multiph. Flow **24**, 387–410 (1998)
64. Osher, S., Sethian, J.A.: Fronts propagating with curvature dependent speed: algorithms based on hamilton-jacobi formulations. J. Comput. Phys. **79**(1), 12–49 (1988)
65. Osher, S., Fedkiw, R.P.: Level set methods: an overview and some recent results. J. Comput. Phys. **169**, 463–502 (2001)
66. Sethian, J.A.: Level Set Methods and Fast Marching Methods. Cambridge University Press, Cambridge (1999)
67. Olsson, E., Kreiss, G.: A conservative level set method for two phase flow. J. Comput. Phys. **210**, 225–246 (2005)
68. Enright, D., Fedkiw, R., Ferziger, J., Mitchell, I.: A hybrid particle level set method for improved interface capturing. J. Comput. Phys. **183**, 83–116 (2002)
69. Sussman, M., Puckett, E.G.: A coupled level set and volume-of-fluid method for computing 3d and axisymmetric incompressible two-phase flows. J. Comput. Phys. **162**(2), 301–337 (2000)
70. Chen, S., Merriman, B., Osher, S., Smereka, P.: A simple level set method for solving Stefan problems. J. Comput. Phys. **135**, 8–29 (1997)
71. Kim, Y.-T., Goldenfeld, N., Dantzig, J.: Computation of dendritic microstructures using a level set method. Phys. Rev. E **62**, 2471–2474 (2000)
72. Gibou, F., Fedkiw, R., Caflisch, R., Osher, S.: A level set approach for the numerical simulation of dendritic growth. J. Sci. Comput. **19**, 183–199 (2003)
73. Yang, Y., Udaykumar, H.: Sharp interface cartesian grid method iii: Solidification of pure materials and binary solutions. J. Comput. Phys. **210**(1), 55–74 (2005)
74. Gibou, F., Fedkiw, R., Cheng, L.-T., Kang, M.: A second-order-accurate symmetric discretization of the Poisson equation on irregular domains. J. Comput. Phys. **176**, 205–227 (2002)
75. Gibou, F., Fedkiw, R.: A fourth order accurate discretization for the Laplace and heat equations on arbitrary domains, with applications to the Stefan problem. J. Comput. Phys. **202**, 577–601 (2005)
76. Chen, H., Min, C., Gibou, F.: A supra-convergent finite difference scheme for the Poisson and heat equations on irregular domains and non-graded adaptive Cartesian grids. J. Sci. Comput. **31**(1–2), 19–60 (2007)
77. Chang, A., Dantzig, J.A., Darr, B.T., Hubel, A.: Modeling the interaction of biological cells with a solidifying interface. J. Comput. Phys. **226**(2), 1808–1829 (2007). doi:10.1016/j.jcp.2007.05.039
78. Aftosmis, M.J., Berger, M.J., Melton, J.E.: Adaptive Cartesian mesh generation. In: CRC Handbook of Mesh Generation (Contributed Chapter) (1998)
79. Brun, E., Guittet, A., Gibou, F.: A local level-set method using a hash table data structure. J. Comput. Phys. **231**, 2528–2536 (2012)

80. Gibou, F., Min, C.: On the performance of a simple parallel implementation of the ILU-PCG for the poisson equation on irregular domains. J. Comput. Phys. **231**(14), 4531–4536 (2012)
81. Losasso, F., Gibou, F., Fedkiw, R.: Simulating water and smoke with an octree data structure. In: ACM Transactions Graph (SIGGRAPH Proceedings) pp. 457–462 (2004)
82. Min, C., Gibou, F., Ceniceros, H.: A supra-convergent finite difference scheme for the variable coefficient Poisson equation on non-graded grids. J. Comput. Phys. **218**(1), 123–140 (2006)
83. Min, C., Gibou, F.: A second order accurate projection method for the incompressible navier-stokes equations on non-graded adaptive grids. J. Comput. Phys. **219**(2), 912–929 (2006)
84. Min, C., Gibou, F.: Geometric integration over irregular domains with application to level-set methods. J. Comput. Phys. **226**(2), 1432–1443 (2007)
85. Min, C., Gibou, F.: Robust second-order accurate discretizations of the multi-dimensional Heaviside and Dirac delta functions. J. Comput. Phys. **227**(22), 9686–9695 (2008)
86. Mirzadeh, M., Theillard, M., Gibou, F.: A second-order discretization of the Nonlinear Poisson–Boltzmann equation over irregular geometries using non-graded adaptive Cartesian grids. J. Comput. Phys. **230**(5), 2125–2140 (2010)
87. Papac, J., Gibou, F., Ratsch, C.: Efficient symmetric discretization for the Poisson, heat and Stefan-type problems with Robin boundary conditions. J. Comput. Phys. **229**(3), 875–889 (2010)
88. Helgadóttir, A., Gibou, F.: A Poisson–Boltzmann solver on irregular domains with Neumann or Robin boundary conditions on non-graded adaptive grid. J. Comput. Phys. **230**(10), 3830–3848 (2011)
89. Miniati, F., Colella, P.: Block structured adaptive mesh and time refinement for hybrid, hyperbolic, n-body systems. J. Comput. Phys. **227**(1), 400–430 (2007)
90. Estep, D., Tavener, S., Wildey, T.: A posteriori error estimation and adaptive mesh refinement for a multiscale operator decomposition approach to fluid-solid heat transfer. J. Comput. Phys. **229**(11), 4143–4158 (2010)
91. Ceniceros, H.D., Nós, R.L., Roma, A.M.: Three-dimensional, fully adaptive simulations of phase-field fluid models. J. Comput. Phys. **229**(17), 6135–6155 (2010)
92. Provatas, N., Goldenfeld, N., Dantzig, J.: Efficient computation of dendritic microstructures using adaptive mesh refinement. Phys. Rev. Lett. **80**, 3308 (1998)
93. Provatas, N., Goldenfeld, N., Dantzig, J.: Adaptive mesh refinement computation of solidification microstructure using dynamic data structures. J. Comput. Phys **148**, 265 (1999)
94. Shu, C.-W., Osher, S.: Efficient implementation of essentially non-oscillatory shock capturing schemes II. J. Comput. Phys. **83**, 32–78 (1989)
95. Liu, X.-D., Osher, S., Chan, T.: Weighted essentially non-oscillatory schemes. J. Comput. Phys. **126**, 202–212 (1996)
96. Strain, J.: Tree methods for moving interfaces. J. Comput. Phys. **151**, 616–648 (1999)
97. Min, C.: Local level set method in high dimension and codimension. J. Comput. Phys. **200**, 368–382 (2004)
98. Fedkiw, R., Aslam, T., Merriman, B., Osher, S.: A non-oscillatory Eulerian approach to interfaces in multimaterial flows (the ghost fluid method). J. Comput. Phys. **152**, 457–492 (1999)
99. Liu, X.D., Fedkiw, R., Kang, M.: A boundary condition capturing method for Poisson's equation on irregular domains. J. Comput. Phys. **154**, 151 (2000)
100. Mirzadeh, M., Theillard, M., Helgadottir, A., Boy, D., Gibou, F.: An adaptive, finite difference solver for the nonlinear poisson-boltzmann equation with applications to biomolecular computations. Commun. Comput. Phys. **13**, 150–173 (2013)
101. Aslam, T.: A partial differential equation approach to multidimensional extrapolation. J. Comput. Phys. **193**, 349–355 (2004)
102. Adalsteinsson, D., Sethian, J.: A fast level set method for propagating interfaces. J. Comput. Phys. **118**, 269–277 (1995)
103. Theillard, M., Rycroft, C.H., Gibou, F.: A multigrid method on non-graded adaptive octree and quadtree Cartesian grids. J. Sci. Comput. **55**, 1–15 (2013)
104. Brandt, A.: Multi-level adaptive solutions to boundary-value problems. Math. Comput. **31**, 333–390 (1977)
105. Mullins, W.W., Sekerka, R.F.: Stability of a planar interface during solidification of a dilute binary alloy. J. Appl. Phys. **5**, 323–329 (1964)
106. Kurz, W., Fisher, D.J.: Fundamentals of Solidification. Trans Tech Publication, Aedermannsdorf, Switzerland (1998)